Complete encapsulation of sulfur through interfacial energy control of sulfur solutions for high-performance Li–S batteries

Donghee Gueon[a], Min-Young Ju[a], and Jun Hyuk Moon[a,1]

[a]Department of Chemical and Biomolecular Engineering, Sogang University, 04107 Seoul, Republic of Korea

Complete encapsulation of high-content sulfur in porous carbon is crucial for high performance Li–S batteries. To this end, unlike conventional approaches to control the pore of carbon hosts, we demonstrate controlling the interfacial energy of the solution in the process of penetrating the sulfur-dissolved solution. We unveil, experimentally and theoretically, that the interfacial energy with the carbon surface of the sulfur solution is the key to driving complete encapsulation of sulfur. In the infiltration of sulfur solutions with *N*-methyl-2-pyrrolidone, we achieve complete encapsulation of sulfur, even up to 85 wt %. The sulfur fully encapsulated cathode achieves markedly high volumetric capacity and stable cycle operation in its Li–S battery applications. We achieve a volumetric capacity of 855 mAh/cm³ at 0.2C and a capacity reduction of 0.071% per cycle up to 300 cycles at 1C.

sulfur encapsulation | interfacial energy | lithium–sulfur batteries | capillary action | high sulfur loading

Next-generation electric vehicles (EVs), hybrid EVs, and energy storage systems require energy storage batteries with high capacity and high energy density (1, 2). Lithium−sulfur (Li–S) batteries are one of the promising candidates because they have a high theoretical capacity (1,675 mAh/g) that enables an energy density (2,600 Wh/kg) more than twice that of conventional lithium−ion batteries (3–6). A common practice for Li–S battery electrodes is to contain sulfur in a porous carbon host (7, 8). Sulfur has a very low electrical conductivity (5×10^{-30} S/cm at 25 °C), and lithium polysulfides (Li PSs) produced during charging/discharging reactions cause dissolution and shuttling in the electrolyte solution (9). Sulfur loading into the porous carbon host (i.e., sulfur loading into the hollow cavity) improves electrical conductivity and prevents the dissolution through physical confinement (10, 11). Previously, much effort was devoted to control the pore structure of carbon or carbon composite in order to securely encapsulate sulfur and form a uniform composite of sulfur and carbon (12–19). Moreover, efforts have also been devoted to designing binder and sulphophilic structure (20, 21).

In contrast to these efforts, a relatively overlooked factor is that the low-to-moderate compatibility of sulfur or sulfur-dissolved solution (typically, a sulfur/CS_2 solution) with carbon causes difficulty in completely loading sulfur into the porous carbon host (22, 23). Recent studies have introduced various metal compounds for improved adsorption of PSs, but, due to their relatively low content, the compatibility with carbon surfaces is still important (24–26). Indeed, molten sulfur shows only partial wetting on the carbon surface (*SI Appendix*, Fig. S1) (27). This property causes highly resistive diffusion of sulfur into the micropores or mesopores of carbon in the traditional melt diffusion processes. Previous results often showed poor penetration of sulfur into the open pores of carbon nanotube (CNT) assembly or carbon particles with hollow cavities (28–30). Meanwhile, even in the case of penetrating the sulfur-dissolved CS_2 solution, the sulfur may not favorably penetrate the porous structure, because the CS_2 has low compatibility with the carbon surface; CS_2 is nonpolar due to its

symmetry molecular structure, and the carbon surface is mildly polar. A sulfur vapor deposition has been proposed to address this issue, but this has limitations in selectively loading sulfur into the porous carbon structure (19). Therefore, a robust and high-fidelity process for complete encapsulation of sulfur, regardless of the carbon or carbon composite host, remains a challenge. This is particularly useful for the fabrication of electrodes containing high amounts of sulfur to achieve ultrahigh energy density.

In this study, we present the control of the interfacial energy of the sulfur solution and thereby completely load a high amount of sulfur into the porous carbon host. We exploit a hollow porous carbon sphere (HPCS) (see *SI Appendix* for synthesis details and productivity of HPCS); this particle has a hierarchical pore structure with a macropore inside and a mesopore in the shell. We apply a mixed solution of isopropyl alcohol (IPA) or *N*-methyl-2-pyrrolidone (NMP) and CS_2 in the preparation of the sulfur solution. The deposition of sulfur by the penetration of each sulfur solution and conventional sulfur/CS_2 solution is compared in Fig. 1. The sulfur/CS_2 solution, due to its low wettability on the carbon surface, causes poor penetration into the pore, resulting in sulfur being deposited outside of the HPCS after evaporation of the solvent, as described in Fig. 1*A*. The solution containing IPA has low sulfur solution−carbon interface energy due to its low surface tension and thereby improves the penetration. NMP is highly compatible with carbon, and, therefore, NMP-containing solutions also show enhanced penetration. Our study reveals that NMP lowers

Significance

Complete encapsulation of high-content sulfur into porous carbon or carbon composites is crucial for high-performance Li–S cells. However, the low-to-moderate compatibility of sulfur-dissolved solution with carbon causes difficulty in completely loading sulfur into the porous host. We control the interfacial energy of the sulfur solution by adding a solvent with high compatibility with the carbon surface. The use of NMP improves the infiltration of sulfur solution effectively, resulting in complete sulfur encapsulation. We observe that the control of sulfur loading greatly affects Li–S battery performance. We identify significantly superior cell performance in the complete encapsulation. Our method can also be applied to effectively load active materials for next-generation energy storage devices.
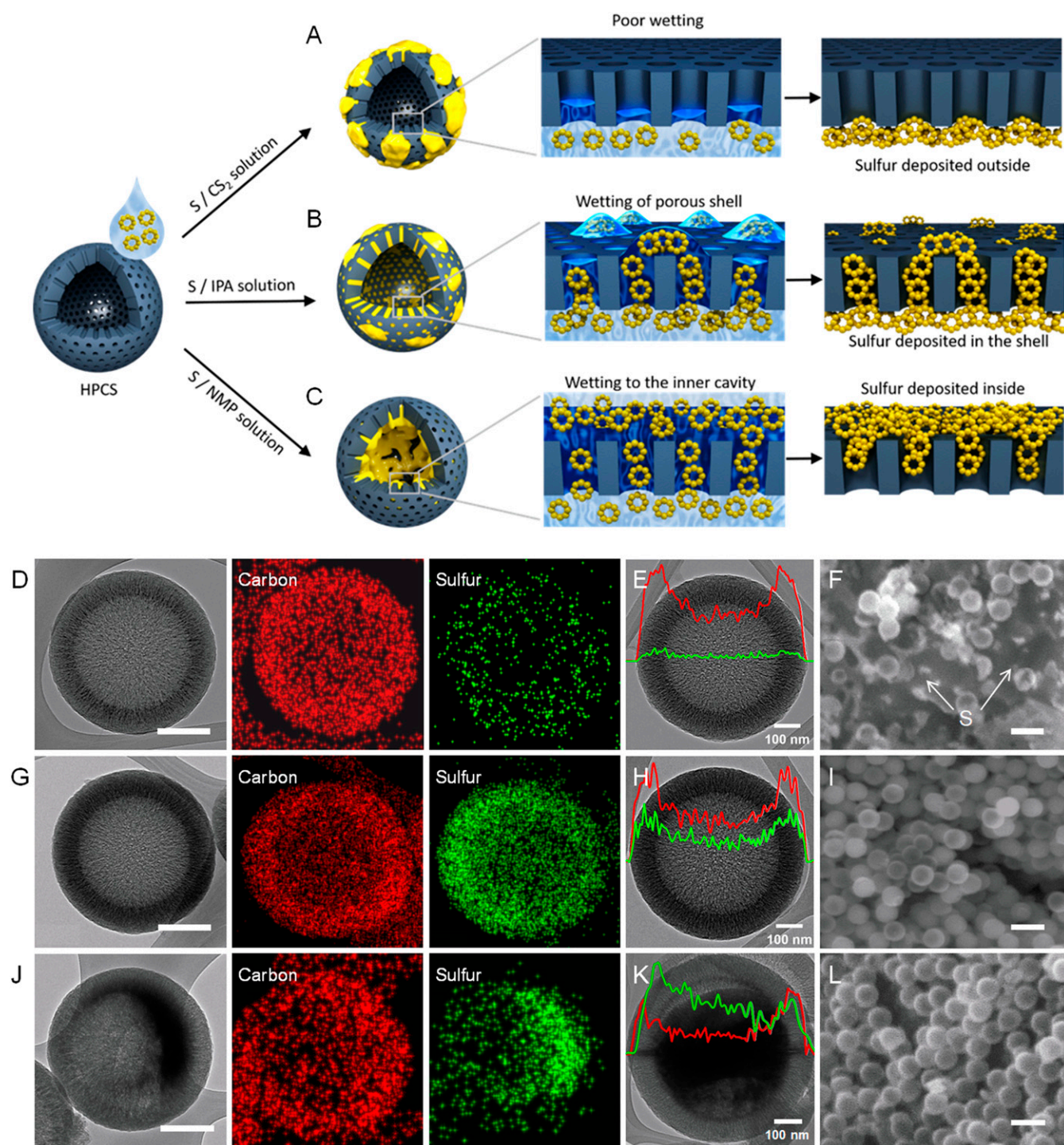
Fig. 1. (*A–C*) (*Left*) Schematic for comparison of penetration of three different sulfur-dissolved solutions into HPCS. (*Right*) (*A*) Penetration of sulfur-dissolved CS$_2$ solution into HPCS and deposition of sulfur after solvent drying. (*B* and *C*) Infiltration of sulfur solution containing IPA or NMP and deposition of sulfur. (*D, G,* and *J*) High-magnification TEM image and EDX elemental mapping of (*D*) S/HPCS (CS$_2$), (*G*) S/HPCS (CS$_2$/IPA), and (*J*) S/HPCS (CS$_2$/NMP). (Scale bar, 200 nm.) (*E, H,* and *K*) High-magnification TEM image and line EDX result for (*E*) S/HPCS (CS$_2$), (*H*) S/HPCS (CS$_2$/IPA), and (*K*) S/HPCS (CS$_2$/NMP); red, carbon; green, sulfur. (*F, I,* and *L*) Low-magnification SEM images of (*F*) S/HPCS (CS$_2$), (*I*) S/HPCS (CS$_2$/IPA), and (*L*) S/HPCS (CS$_2$/NMP). (Scale bar, 1 μm.) The S content for all samples was 75 wt %, which was confirmed by thermogravimetric analysis (TGA) (*SI Appendix*, Fig. S11A).

interfacial energy more than IPA, resulting in sulfur deposition only in the porous shell for the IPA solution (Fig. 1*B*) and sulfur deposition into the hollow cavity (i.e., complete encapsulation of sulfur) in the NMP solution (Fig. 1*C*). We apply sulfur-loaded carbon hosts prepared with each sulfur solution to the cathode of a Li–S cell. We achieve the best performance in the cathode with the most secure sulfur loading prepared using the NMP-containing solution; this cell achieves significantly higher volumetric capacity and stable cycle operation.

HPCSs are formed by first forming a silica core as a seed with the Stöber method, forming a silica layer containing the polymer

resorcinol formaldehyde (RF), and then carbonizing the RF and selectively removing the SiO$_2$. Detailed synthetic procedures and scanning electron microscopy (SEM) images of the particles at each step are given in *SI Appendix*, Fig. S2. HPCSs have a mesopore carbon shell and macropores inside; the internal macropores of HPCSs provide a reservoir for high sulfur loading, and the mesopore shell can inhibit the dissolution of Li PSs out of the spheres (31, 32). *SI Appendix*, Fig. S3 shows the HPCS has a diameter of about 600 nm and a mesopore shell with a pore size of about 5 nm. The transmission electron microscopy (TEM) image also shows pore channels aligned in the radial direction. The X-ray diffraction (XRD) spectrum shown in *SI Appendix*, Fig. S4 reveals the glassy carbon character of HPCSs (33).

We wet the carbon sphere with a sulfur solution and evaporate the solvent to deposit the sulfur. CS$_2$ is widely used because it has uniquely high solubility for sulfur (~450 mg/mL at 25 °C) (34). The TEM image, its elemental mapping, and the line profile of sulfur for a sample prepared by infiltration of sulfur-dissolved pure CS$_2$ solution show that only a trace amount of sulfur is loaded in the porous shell and macropore cavity (Fig. 1 D and E). The SEM image of Fig. 1F clearly shows the residue of sulfur present on the outside of the particle. Previous studies have also observed imperfect sulfur loading into carbon pores (35, 36). Furthermore, even in the melt diffusion of sulfur, conventionally applied, we observe that sulfur does not penetrate into the pores in the sphere (*SI Appendix*, Fig. S5). We surmise that this is due to the unfavorable wetting of CS$_2$ on the carbon surface, resulting in less infiltration of sulfur into the carbon pores. Indeed, as shown later in Fig. 2A, CS$_2$ shows only partial wetting on the carbon surface; the contact angle of CS$_2$ on a carbon surface was measured to be 53°.

Now we apply binary solvents to improve wetting of the sulfur solution on the carbon surface. We chose IPA as an additional solvent since it has a very low surface tension of 22 mN/m and chose NMP since it is widely used as a solvent capable of dispersing CNTs or graphene (37–39). Here, we prepared a binary solvent containing 40% IPA or NMP in CS$_2$; each solution has a solubility comparable to that of CS$_2$ (*SI Appendix*, Fig. S6). TEM images of sulfur-loaded HPCS (S/HPCS) prepared using these mixture solutions and the elemental mapping of S and C in these images are shown in Fig. 1 G and J, respectively. Fig. 1 H and K shows line profiles of the elemental mapping of S/HPCS prepared using the solutions containing IPA and NMP, respectively. Using mixed solvents clearly produces different sulfur loadings from the loading obtained using pure CS$_2$. In S/HPCS prepared using CS$_2$/IPA, sulfur is observed in the porous shell. With the CS$_2$/NMP solvent, the sulfur is carried into the macropores (*SI Appendix*, Fig. S7) for more TEM images of many S/HPCS particles prepared using the sulfur-dissolved CS$_2$/NMP solution). In the SEM images in Fig. 1 I and L, no sulfur residue is visible around the HPCSs fabricated with the IPA- or NMP-containing solution. These results confirm that the CS$_2$/IPA and CS$_2$/NMP solutions lead to the more complete infiltration of sulfur-dissolved solvent into the pores of HPCSs. The XRD spectrum shown in *SI Appendix*, Fig. S8 reveals the sulfur character of S/HPCS (CS$_2$/NMP) (40, 41).

The different loading of sulfur for the three solutions can also be confirmed by Brunauer–Emmett–Teller (BET) pore analysis of S/HPCS (*SI Appendix*, Fig. S9). The S/HPCS (CS$_2$) sample shows little N$_2$ adsorption, reflecting the complete coverage of HPCS by the sulfur residue. The S/HPCS (CS$_2$/NMP) exhibits adsorption in mesopore, while the S/HPCS (CS$_2$/IPA) shows nonporous characteristics. This can be explained by the fact that, in the S/HPCS (CS$_2$/IPA), sulfur is deposited in the shell to block the mesopore, whereas, in the S/HPCS (CS$_2$/NMP), the adsorption profile indicates the presence of mesopore shell due to the deposition of sulfur in the inner hollow cavity.

To illustrate the difference in infiltration depending on the solvent composition, we analyze the capillary action of the solution inside the mesopore shell of HPCS. In such small pores, the infiltration is dominated by capillary pressure (42). The capillary pressure force depends on the contact angle with the surface and the interfacial tension of the liquid (i.e., $\gamma_{lv} \cos\theta$). The contact angles (θ) of CS$_2$, CS$_2$/IPA, and CS$_2$/NMP solutions on a flat carbon surface are measured to be 53°, 17°, and 17°, respectively, as observed in Fig. 2A. The value of γ_{lv} is calculated by the lever rule considering the mixing ratio, yielding 32 mN/m for CS$_2$, 29 mN/m for CS$_2$/IPA, and 35 mN/m for CS$_2$/NMP (37). Details of the calculation of the capillary pressure are given in *SI Appendix, Supplementary Note #1*. Then, the capillary pressures of CS$_2$/NMP and CS$_2$/IPA are ~1.7 times and 1.4 times larger, respectively, than CS$_2$. These results explain the significantly improved infiltration of the solution containing IPA and NMP into the carbon pores compared to the CS$_2$ solution and also explain the improved infiltration in solutions containing NMP over IPA.

This calculation shows that the penetration of the liquid into the carbon pores is determined by the contribution of the contact angle and the interfacial tension of the liquid. This indicates that the interfacial energy of the liquid/solid is the term that determines the penetration; the interfacial energy, γ_{sl}, is equal to the surface energy of the carbon, $\gamma_{sv} - \gamma_{lv} \cos\theta$, from the Young's equation under partial wetting conditions (42). The γ_{sv} of carbon was reported to be ~39.5 mN/m for glassy carbon (43). The γ_{sl} value obtained by subtracting $\gamma_{lv} \cos\theta$ from this value is 20.2 mN/m for CS$_2$, 11.8 mN/m for CS$_2$/IPA, and 6 mN/m for CS$_2$/NMP (Table 1). The γ_{sl} values were further confirmed by simulation using Surface Evolver software (*SI Appendix, Supplementary Note #2*); we simulated a droplet contacting the carbon surface with minima in the energy landscape satisfying the equilibrium of the three forces in Young's equation. We obtained γ_{sl} values of 21.5, 11.5, and 5.5 mN/m for CS$_2$, CS$_2$/IPA and CS$_2$/NMP, respectively, in the simulation, which agree with the values in the experiment. Compared to the IPA solution, the NMP solution exhibits a similar contact angle but has a much lower interfacial energy, so it penetrates more favorably into the macropore cavity of the interior of the carbon particles. We further applied other solvents (ethanol and *N,N*-dimethylformamide) to confirm the hypothesis that the penetration of sulfur-dissolved solution is determined by interfacial energy. Ethanol has a surface tension similar to IPA, and *N,N*-dimethylformamide has interfacial energy with carbon which is similar to NMP. The results show that CS$_2$/ethanol shows sulfur loading in the shell similar to IPA, and CS$_2$/DMF confirms the deposition of sulfur into the hollow cavity (*SI Appendix, Supplementary Note #3*).

We prepared a Li−S battery cell containing S/HPCS (CS$_2$), S/HPCS (CS$_2$/IPA), or S/HPCS (CS$_2$/NMP) cathode. First, we
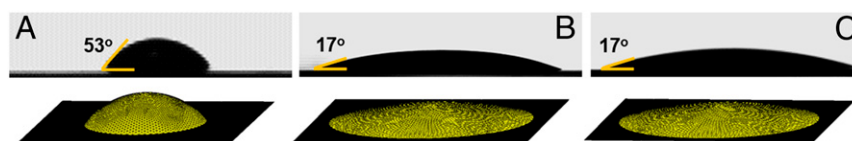

Fig. 2. Contact angle of (A) CS$_2$, (B) CS$_2$/IPA (7:3 mol %), and (C) CS$_2$/NMP (7:3 mol %) on a glassy carbon substrate and simulation images of wetting on the carbon surface of each solution drop.

Table 1. Characterization of CS₂, CS₂/IPA, and CS₂/NMP solvents on glassy carbon substrate

Solvents	CS₂, mN/m	CS₂/IPA, mN/m	CS₂/NMP, mN/m
γ_{lv}	32 (60)	29 (61)	35 (62)
$\gamma_{lv} \cos\theta$	19.3	27.7	33.5
γ_{sv} (43)	39.5	39.5	39.5
$\gamma_{sl} = \gamma_{sv} - \gamma_{lv} \cos\theta$	20.2	11.8	6

obtained cyclic voltammetric curves in the 1.7- to 2.8-V (vs. Li/Li⁺) region at various scan rates, as observed in Fig. 3 A–C. These curves show cathodic peaks at 2.4 V and 1.95 V on the reduction curves, which are related to reduction reactions of $S_8 + 4Li^+ + 4e^- \rightarrow 2Li_2S_4$ (C₁) and $2Li_2S_4 + 12Li^+ + 12e^- \rightarrow 8Li_2S$ (C₂), respectively. Additionally, the anodic peak near 2.5 V is related to the reverse reaction of Li PS: Li_2S_2/Li_2S to S_8 (44, 45). The response of the peak current to the scan rate is related to the rate of the sulfur transformation reaction. We obtained the relative the diffusivity of Li ions (D_{Li+}) using the modified Randles–Sevcik relationship (5).

$$D_{Li+} \propto \frac{I_p^2}{S^2 n^2 C_{Li}^2 v},$$ [1]

where I_p is the peak current, n is the charge transfer number, S is the geometric area of the active electrode, C_{Li} is the concentration of lithium ions in the cathode, and v is the potential scan rate. Here, D_{Li+} includes the diffusion of Li⁺ in solution to the surface of the sulfur deposit and the quasi−solid-state/solid-state diffusion in the LiPS layer formed on the S surface (46, 47). The D_{Li+} of each sample at each redox peak is compared as shown in Fig. 3D; for every redox peak, S/HPCS (CS₂/NMP) and S/HPCS (CS₂/IPA)

show a much higher value than S/HPCS (CS₂), revealing the fast reaction kinetics achieved with the S/HPCS (CS₂/NMP) and S/HPCS (CS₂/IPA) electrodes (5). In particular, we observe significant differences between each sample for the C₂ reaction. Poor diffusion in S/HPCS (CS₂) samples is responsible for slow solid-state diffusion in bulk sulfur residues (46, 48, 49). In S/HPCS (CS₂/IPA), sulfur is encapsulated in a microdomain in a porous shell, but there may be a large delay in the liquid-phase diffusion of Li⁺ in sulfur-clogged mesopores (50). In the S/HPCS (CS₂/NMP), a thin layer of sulfur deposited on the inner wall of the porous shell, which allows rapid diffusion of Li⁺ into open pores of the shell (51). A comparison of the charge diffusion for these samples is described in detail in *SI Appendix, Supplementary Note #4.*

Fig. 3E compares the electrochemical impedance spectra of these electrodes. The semicircle corresponds to the charge transfer resistance (R_{ct}) for the electroredox reaction at the electrode/electrolyte interface, and the straight line in the high-frequency region is the Warburg impedance and corresponds to Liion diffusion. The S/HPCS (CS₂/NMP) electrode shows the smallest semicircle and also the straightest line with the steepest slope; this confirms the smallest R_{ct} value and the fastest diffusion of S/HPCS (CS₂/NMP).

Second, the galvanostatic charge/discharge characteristics of the S/HPCS (CS₂), S/HPCS (CS₂/IPA), and S/HPCS (CS₂/NMP) cathodes are compared in Fig. 4 A–C. Two representative plateaus are observed in the discharge voltage profile (Fig. 4 A–C). The first plateau at 2.3 V shows the reduction from solid S_8 to higher-order Li PSs (Li_2S_n, $n = 4$ to 8), and the second plateau at 2.1 V shows the reduction to insoluble Li_2S_2 and Li_2S. Ideally, the capacity from the second reaction is 3 times the capacity from the first reaction. However, since the reaction related to the second plateau, including nucleation and solid-state charge diffusion, is sluggish, the capacity ratio (Q_2/Q_1) for the first and second
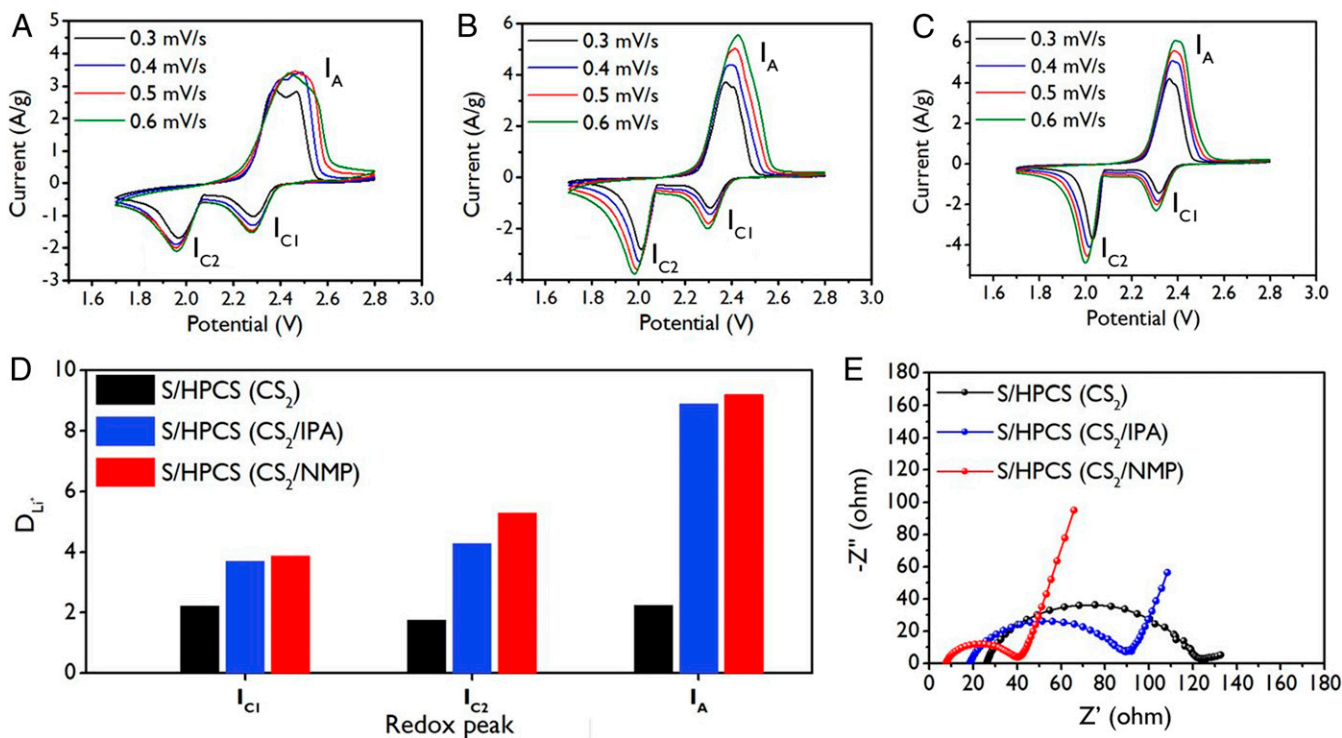

Fig. 3. (*A*–*C*) Cyclic voltammetry of (*A*) S/HPCS (CS₂), (*B*) S/HPCS (CS₂/IPA), and (*C*) S/HPCS (CS₂/NMP) cathodes between 2.8 V and 1.7 V at various scan rates from 0.3 mV/s to 0.6 mV/s. (*D*) Relative diffusivity of Li⁺ ion for each cathodic and anodic reaction. (*E*) Nyquist plots of S/HPCS(CS₂), S/HPCS(CS₂/IPA), and S/HPCS(CS₂/NMP) cathodes.
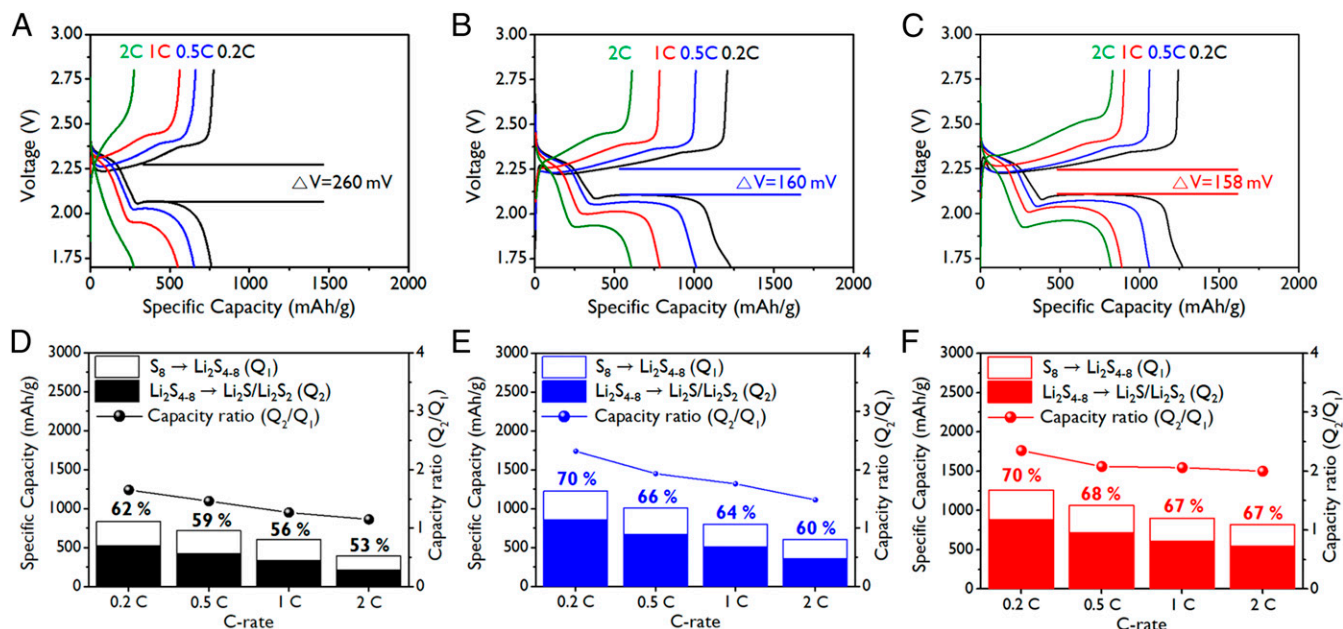
Fig. 4. (*A–C*) Charge/discharge voltage profiles of the (*A*) S/HPCS (CS$_2$), (*B*) S/HPCS (CS$_2$/IPA), and (*C*) S/HPCS (CS$_2$/NMP) cathodes at first cycle of various C rates from 0.2C to 2C. (*D–F*) Capacity contribution of high-order PS conversion (Q$_1$) and low-order PS conversion (Q$_2$) and the Q$_2$/Q$_1$ ratio at various C rates for the (*D*) S/HPCS (CS$_2$), (*E*) S/HPCS (CS$_2$/IPA), and (*F*) S/HPCS (CS$_2$/NMP) cathodes.

plateaus is less than 3 (25). We compared the ratio of Q$_2$/Q$_1$ at various C rates for each electrode, as observed in Fig. 4 *D–F*. As predicted, the S/HPCS (CS$_2$) electrode exhibits a very small ratio below 1.5, deviating considerably from the ideal value: Low utilization of sulfur by incomplete encapsulation into carbon pore is observed. S/HPCS (CS$_2$/NMP) shows a higher ratio than S/HPCS (CS$_2$/IPA), especially at higher C rates; at 2C, the ratio for S/HPCS (CS$_2$/NMP) is 2, but the ratio for S/HPCS (CS$_2$/IPA) is 1.5. In S/HPCS (CS$_2$/IPA), in which the sulfur is loaded in the mesopore shell, there may be pore clogging during the discharging reaction. It has been observed that pore clogging in a zeolite-templated microporous carbon host results in low performance at a high rate (52). S/HPCS (CS$_2$/NMP) is capable of ion transfer to the interior via the mesopore shell, which may allow relatively high utilization of sulfur. Moreover, the PS ions confined in the macropore cavities inside may also promote the nucleation reaction (53).

Fig. 5*A* shows the cycle performance of S/HPCS (CS$_2$), S/HPCS (CS$_2$/IPA), and S/HPCS (CS$_2$/NMP) cells at a C rate of 1C. The sulfur content was 75 wt %, and the sulfur loading for the electrodes was ~1 mg/cm^2. S/HPCS (CS$_2$/NMP) showed markedly outstanding retention of ~89% with a capacity of 750 mAh/g at 100 cycles; S/HPCS (CS$_2$/IPA) showed a retention of ~77%, and S/HPCS (CS$_2$) had a very low retention of 44%. We also present a comparison of S/HPCS (CS$_2$/NMP) with S/HPCS by conventional melt diffusion in *SI Appendix*, Fig. S10. The S/HPCS (CS$_2$/NMP) cell shows faster kinetics and higher sulfur utilization for sulfur redox reactions; the poor performance of the melt diffusion S/HPCS may be responsible for poor penetration into the mesoporous shell due to the high viscosity of the molten sulfur.

Furthermore, we compared the cycle performance of each cathode cell at a very high sulfur content of 85 wt % (*SI Appendix*, Fig. S11*B*), as shown in Fig. 5*B*. Note that a sulfur content of 85 wt % should contain approximately twice the volume of sulfur in a 75 wt % loading. Previous results for a hollow carbon sphere-based Li−S cell typically applied a sulfur loading of 60 to 75 wt % (*SI Appendix*, Table S1). We observe the sulfur residue around the HPCSs for the S/HPCS (CS$_2$/IPA) sample but not the S/HPCS (CS$_2$/NMP) sample (*SI Appendix*, Fig. S12). This

indicates that S/HPCS (CS$_2$/NMP) had a complete penetration of sulfur into the hollow carbon. In the case of S/HPCS (CS$_2$/IPA), the sulfur is deposited in a mesopore shell with a limited volume, thus leading to an incomplete loading in the high sulfur content. The S/HPCS (CS$_2$/NMP) cell still displays a stable capacity retention of 80%, but the S/HPCS (CS$_2$/IPA) cell shows the retention of only 64%. In the case of the S/HPCS (CS$_2$/NMP), the sulfur redox reaction may occur only in the inner cavity, thereby limiting the shuttling of PS ions in the cavity, resulting in excellent capacity retention (54). In contrast, the S/HPCS (CS$_2$/IPA) shows poor retention due to incomplete utilization of sulfur residues. The long-term cycle performance of S/HPCS (CS$_2$/NMP) cells is recorded up to 300 cycles as shown in Fig. 5*C*. The cell shows a reduction of only 0.071% per cycle until reaching 300 cycles after a reduction in capacity of ~0.3% per cycle for the initial 40 cycles. Fig. 5 *C*, *Inset* is an image of 30 LEDs lit for 20 min with constant brightness; this result confirms the stable operation of the S/HPCS (CS$_2$/NMP) cell. Fig. 5 *D* and *E* compares the morphologies before and after charging/discharging for S/HPCS (CS$_2$/NMP) and S/HPCS (CS$_2$) electrodes, respectively. Unlike the S/HPCS (CS$_2$), where the formation of irreversible Li$_2$S$_2$/Li$_2$S precipitation on the surface of the carbon spheres is prominent, the S/HPCS (CS$_2$/NMP) shows carbon spheres with no surface residues even after the cycle (*SI Appendix*, Fig. S13).

Complete encapsulation of sulfur in S/HPCS (CS$_2$/NMP) enables the achievement of high volumetric capacity of Li−S cell. We evaluate the cycle performance of an electrode cell with a cathode sulfur density of 0.62 g/cm^3 at a high sulfur loading of 4 mg/cm^2. The volumetric capacity is obtained by multiplying the gravimetric capacity by the sulfur loading and dividing this value by the electrode thickness (65 μm; *SI Appendix*, Fig. S14), as shown in Fig. 5*F*. The cell shows an initial gravimetric capacity of 1,388 mAh/g at 0.2C and a retention rate of 86% for 100 cycles at 0.5C. The calculated volumetric capacity is also displayed, showing 855 mAh/cm^3 and 652 mAh/cm^3 at 0.2C and 0.5C, respectively. Compared with recent results (55–59) as shown in Fig. 5*G*, the S/HPCS (CS$_2$/NMP) cell exhibits high volumetric capacity, even at high sulfur loading.
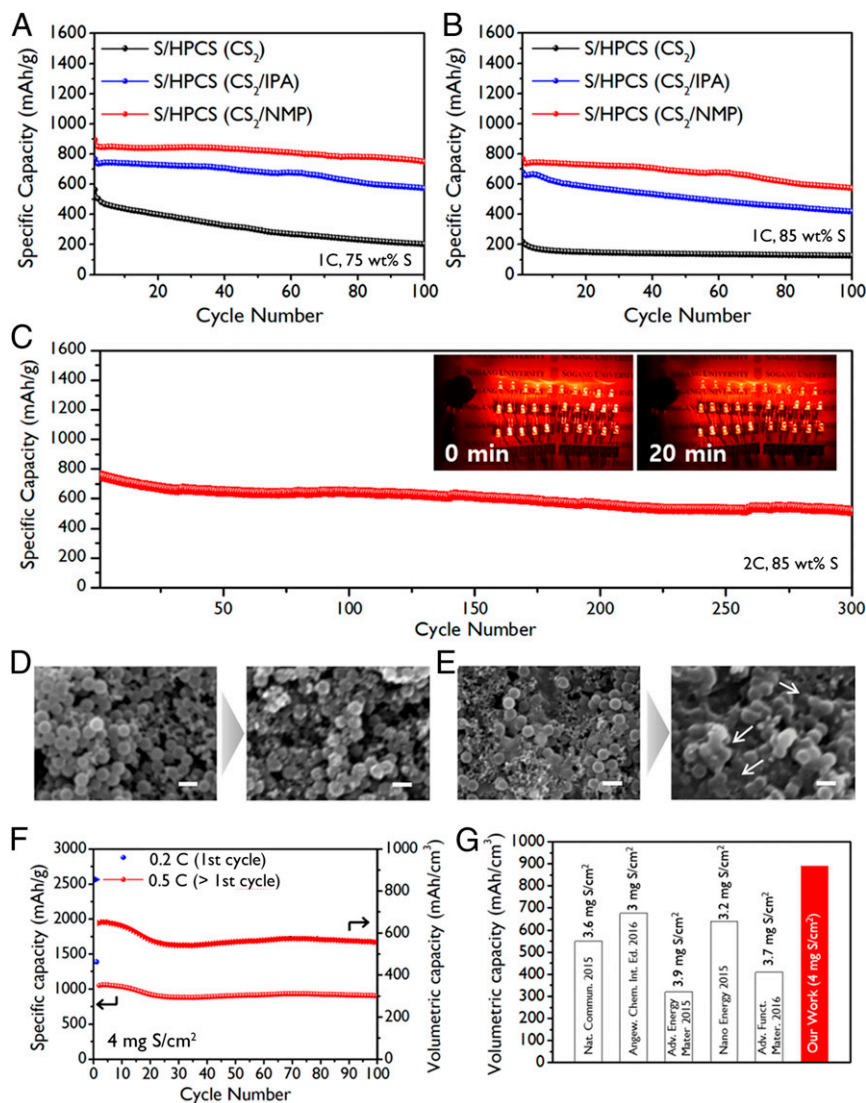
Fig. 5. (*A* and *B*) Cycling performance of S/HPCS (CS$_2$), S/HPCS (CS$_2$/IPA), and S/HPCS (CS$_2$/NMP) electrode cells at (*A*) 1C with 75 wt % sulfur content and at (*B*) 1C with 85 wt % sulfur content. These results display data after several cycles of activation. (*C*) Cycling performance of the S/HPCS (CS$_2$/NMP) electrode cell at 2C with 85 wt % sulfur content. *Inset* is a 30-LED array with one S/HPCS (CS$_2$/NMP) electrode cell. (*D* and *E*) SEM images of (*D*) S/HPCS (CS$_2$/NMP) electrode and (*E*) S/HPCS (CS$_2$) electrode before and after 50 cycles, respectively. (Scale bar, 1 μm.) The arrow indicates a Li$_2$S/Li$_2$S residue. (*F*) Specific and volumetric capacity of S/HPCS (CS$_2$/NMP) electrode cell at 0.5C with one cycle activation step at 0.2C. (*G*) Comparison of volumetric capacity values in our electrode and recent results using similar sulfur loading (55–59).

In conclusion, we demonstrate controlled sulfur loading into HPCSs by controlling the interfacial energy of sulfur-dissolved solution. The widely used sulfur/CS$_2$ solution does not easily penetrate porous carbon, due to the high interfacial energy of CS$_2$, resulting in a bulk sulfur residue. We find that the use of a mixed solution containing IPA or NMP significantly improves the infiltration of the solution into the pores by improving wetting with the carbon surface. In particular, the use of NMP with low interfacial energy with carbon can improve infiltration more effectively, resulting in complete sulfur encapsulation. We further observed that the control of sulfur loading greatly affects Li–S battery performance. Specifically, the rate and reversibility of the sulfur transformation reaction depend largely on the location of the sulfur loading. We identify significantly superior cell performance (reversible capacity and capacity retention) in the loading of sulfur into the internal macropore of HPCS. Our method can be applied as a facile but precise control technique for the

complete encapsulation of sulfur to a host with a variety of surfaces and morphologies.

Materials and Methods

HPCS was prepared by first forming a SiO$_2$ core and a formaldehyde–resorcinol polymer shell, heat-treating the particles at high temperature, and then removing SiO$_2$. Sulfur deposition was obtained by wetting HPCS with sulfur solution (solution in which sulfur is dissolved in CS$_2$, CS$_2$/IPA, or CS$_2$/NMP). All procedures and analysis of HPCS samples are described in detail in *SI Appendix, Methods*. The fabrication and evaluation of lithium–sulfur battery cells is also presented in *SI Appendix*.

Data Availability. All data needed to evaluate the conclusions in this paper are available in the main text or in *SI Appendix*.

1. J. W. Choi, D. Aurbach, Promise and reality of post-lithium-ion batteries with high energy densities. *Nat. Rev. Mater.* **1**, 16013 (2016).

2. W. Li et al., High-performance hollow sulfur nanostructured battery cathode through a scalable, room temperature, one-step, bottom-up approach. *Proc. Natl. Acad. Sci. U.S.A.* **110**, 7148–7153 (2013).

3. C. Tang et al., CaO-templated growth of hierarchical porous graphene for high-power lithium–sulfur battery applications. *Adv. Funct. Mater.* **26**, 577–585 (2016).

4. S. Bai, X. Liu, K. Zhu, S. Wu, H. Zhou, Metal–organic framework-based separator for lithium–sulfur batteries. *Nat. Energy* **1**, 16094 (2016).

5. G. Zhou et al., Catalytic oxidation of Li2S on the surface of metal sulfides for Li–S batteries. *Proc. Natl. Acad. Sci. U.S.A.* **114**, 840–845 (2017).

6. H. Ye et al., Amorphous MoS$_3$ as the sulfur-equivalent cathode material for room-temperature Li–S and Na–S batteries. *Proc. Natl. Acad. Sci. U.S.A.* **114**, 13091–13096 (2017).

7. Y. Chen, S. Choi, D. Su, X. Gao, G. Wang, Self-standing sulfur cathodes enabled by 3D hierarchically porous titanium monoxide-graphene composite film for high-performance lithium-sulfur batteries. *Nano Energy* **47**, 331–339 (2018).

8. W. Bao et al., Facile synthesis of crumpled nitrogen-doped MXene nanosheets as a new sulfur host for lithium–sulfur batteries. *Adv. Energy Mater.* **8**, 1702485 (2018).

9. G. Li et al., Three-dimensional porous carbon composites containing high sulfur nanoparticle content for high-performance lithium-sulfur batteries. *Nat. Commun.* **7**, 10601 (2016).

10. Z. W. Seh et al., Two-dimensional layered transition metal disulphides for effective encapsulation of high-capacity lithium sulphide cathodes. *Nat. Commun.* **5**, 5017 (2014).

11. J. Xu et al., MOF-derived porous N–Co 3 O 4@ N–C nanododecahedra wrapped with reduced graphene oxide as a high capacity cathode for lithium–sulfur batteries. *J. Mater. Chem. A Mater. Energy Sustain.* **6**, 2797–2807 (2018).

12. S. Zheng et al., Copper-stabilized sulfur-microporous carbon cathodes for Li–S batteries. *Adv. Funct. Mater.* **24**, 4156–4163 (2014).

13. Y. Xu et al., Confined sulfur in microporous carbon renders superior cycling stability in Li/S batteries. *Adv. Funct. Mater.* **25**, 4312–4320 (2015).

14. H. Wang, C. Zhang, Z. Chen, H. K. Liu, Z. Guo, Large-scale synthesis of ordered mesoporous carbon fiber and its application as cathode material for lithium–sulfur batteries. *Carbon* **81**, 782–787 (2015).

15. L. Zhang et al., High-content of sulfur uniformly embedded in mesoporous carbon: A new electrodeposition synthesis and an outstanding lithium–sulfur battery cathode. *J. Mater. Chem. A Mater. Energy Sustain.* **5**, 5905–5911 (2017).

16. K. Mi, Y. Jiang, J. Feng, Y. Qian, S. Xiong, Hierarchical carbon nanotubes with a thick microporous wall and inner channel as efficient scaffolds for lithium–sulfur batteries. *Adv. Funct. Mater.* **26**, 1571–1579 (2016).

17. P. Strubel et al., ZnO hard templating for synthesis of hierarchical porous carbons with tailored porosity and high performance in lithium-sulfur battery. *Adv. Funct. Mater.* **25**, 287–297 (2015).

18. H. Li et al., Dense integration of graphene and sulfur through the soft approach for compact lithium/sulfur battery cathode. *Nano Energy* **12**, 468–475 (2015).

19. M. Li, R. Carter, A. Douglas, L. Oakes, C. L. Pint, Sulfur vapor-infiltrated 3D carbon nanotube foam for binder-free high areal capacity lithium–sulfur battery composite cathodes. *ACS Nano* **11**, 4877–4884 (2017).

20. G. Zhou et al., Sulfiphilic nickel phosphosulfide enabled Li2S impregnation in 3D graphene cages for Li–S batteries. *Adv. Mater.* **29**, 1603366 (2017).

21. G. Zhou et al., An aqueous inorganic polymer binder for high performance lithium–sulfur batteries with flame-retardant properties. *ACS Cent. Sci.* **4**, 260–267 (2018).

22. R. Fanelli, The surface tension of sulfur. *J. Am. Chem. Soc.* **72**, 4016–4018 (1950).

23. X. Fan et al., A general dissolution–recrystallization strategy to achieve sulfur-encapsulated carbon for an advanced lithium–sulfur battery. *J. Mater. Chem. A Mater. Energy Sustain.* **6**, 11664–11669 (2018).

24. X. Liang et al., A highly efficient polysulfide mediator for lithium-sulfur batteries. *Nat. Commun.* **6**, 5682 (2015).

25. T. An et al., MnO modified carbon nanotubes as a sulfur host with enhanced performance in Li/S batteries. *J. Mater. Chem. A Mater. Energy Sustain.* **4**, 12858–12864 (2016).

26. Y. Zhong et al., Confining sulfur in integrated composite scaffold with highly porous carbon fibers/vanadium nitride arrays for high-performance lithium–sulfur batteries. *Adv. Funct. Mater.* **28**, 1706391 (2018).

27. J. Scholz et al., Severe loss of confined sulfur in nanoporous carbon for Li–S batteries under wetting conditions. *ACS Energy Lett.* **3**, 387–392 (2018).

28. L. Sun et al., Sulfur embedded in a mesoporous carbon nanotube network as a binder-free electrode for high-performance lithium–sulfur batteries. *ACS Nano* **10**, 1300–1308 (2016).

29. Z. Yuan et al., Hierarchical free-standing carbon-nanotube paper electrodes with ultrahigh sulfur-loading for lithium–sulfur batteries. *Adv. Funct. Mater.* **24**, 6105–6112 (2014).

30. D. Gueon et al., Spherical macroporous carbon nanotube particles with ultrahigh sulfur loading for lithium–sulfur battery cathodes. *ACS Nano* **12**, 226–233 (2018).

31. G. He et al., Tailoring porosity in carbon nanospheres for lithium-sulfur battery cathodes. *ACS Nano* **7**, 10920–10930 (2013).

32. M. Li et al., Gas Pickering emulsion templated hollow carbon for high rate performance lithium sulfur batteries. *Adv. Funct. Mater.* **26**, 8408–8417 (2016).

33. P. Lu, Y. Sun, H. Xiang, X. Liang, Y. Yu, 3D amorphous carbon with controlled porous and disordered structures as a high-rate anode material for sodium-ion batteries. *Adv. Energy Mater.* **8**, 1702434 (2018).

34. C. Oh et al., Enhanced Li–S battery performance based on solution-impregnation-assisted sulfur/mesoporous carbon cathodes and a carbon-coated separator. *J. Mater. Chem. A Mater. Energy Sustain.* **5**, 5750–5760 (2017).

35. S. S. Zhang, Does the sulfur cathode require good mixing for a liquid electrolyte lithium/sulfur cell? *Electrochem. Commun.* **31**, 10–12 (2013).

36. Y. Liu, H. Zhan, Y. Zhou, Investigation of S/C composite synthesized by solvent exchange method. *Electrochim. Acta* **70**, 241–247 (2012).

37. J. Shereshefsky, A theory of surface tension of binary solutions: I. Binary liquid mixtures of organic compounds. *J. Colloid Interface Sci.* **24**, 317–322 (1967).

38. J. Chen et al., Surface energy of amorphous carbon films containing iron. *J. Appl. Phys.* **89**, 7814–7819 (2001).

39. X. Zhao et al., Root-like porous carbon nanofibers with high sulfur loading enabling superior areal capacity of lithium sulfur batteries. *Carbon* **128**, 138–146 (2018).

40. X. Wang, Z. Zhang, Y. Qu, Y. Lai, J. Li, Nitrogen-doped graphene/sulfur composite as cathode material for high capacity lithium–sulfur batteries. *J. Power Sources* **256**, 361–368 (2014).

41. H.-C. Youn et al., Phase transition method to form Group 6A nanoparticles on carbonaceous templates. *ACS Nano* **8**, 2279–2289 (2014).

42. P.-G. De Gennes, F. Brochard-Wyart, D. Quéré, *Capillarity and Wetting Phenomena: Drops, Bubbles, Pearls, Waves,* (Springer Science & Business Media, 2013).

43. T. Svitova, R. Hill, Y. Smirnova, A. Stuermer, G. Yakubov, Wetting and interfacial transitions in dilute solutions of trisiloxane surfactants. *Langmuir* **14**, 5023–5031 (1998).

44. Z. Yuan et al., Powering lithium–sulfur battery performance by propelling polysulfide redox at sulfiphilic hosts. *Nano Lett.* **16**, 519–527 (2016).

45. Y. Chen et al., Co-Fe mixed metal phosphide nanocubes with highly interconnected-pore architecture as an efficient polysulfide mediator for lithium-sulfur batteries. *ACS Nano* **13**, 4731–4741 (2019).

46. H. Chen et al., Monodispersed sulfur nanoparticles for lithium-sulfur batteries with theoretical performance. *Nano Lett.* **15**, 798–802 (2015).

47. N. Li et al., An aqueous dissolved polysulfide cathode for lithium–sulfur batteries. *Energy Environ. Sci.* **7**, 3307–3312 (2014).

48. D.-W. Wang et al., Carbon-sulfur composites for Li–S batteries: Status and prospects. *J. Mater. Chem. A Mater. Energy Sustain.* **1**, 9382–9394 (2013).

49. X. Ji, L. F. Nazar, Advances in Li–S batteries. *J. Mater. Chem.* **20**, 9821–9826 (2010).

50. B. Zhang, X. Qin, G. Li, X. Gao, Enhancement of long stability of sulfur cathode by encapsulating sulfur into micropores of carbon spheres. *Energy Environ. Sci.* **3**, 1531–1537 (2010).

51. J. Song et al., Rational design of free-standing 3D porous MXene/rGO hybrid aerogels as polysulfide reservoirs for high-energy lithium–sulfur batteries. *J. Mater. Chem. A Mater. Energy Sustain.* **7**, 6507–6513 (2019).

52. H. Noh, S. Choi, H. G. Kim, M. Choi, H.-T. Kim, Size tunable zeolite-templated carbon as microporous sulfur host for lithium-sulfur batteries. *ChemElectroChem* **6**, 558–565 (2019).

53. W. Wu et al., Biomimetic bipolar microcapsules derived from *Staphylococcus aureus* for enhanced properties of lithium–sulfur battery cathodes. *Adv. Energy Mater.* **8**, 1702373 (2018).

54. D. Su, M. Cortie, H. Fan, G. Wang, Prussian blue nanocubes with an open framework structure coated with PEDOT as high-capacity cathodes for lithium-sulfur batteries. *Adv. Mater.* **29**, 1700587 (2017).

55. Z. Li, J. T. Zhang, Y. M. Chen, J. Li, X. W. D. Lou, Pie-like electrode design for high-energy density lithium-sulfur batteries. *Nat. Commun.* **6**, 8850 (2015).

56. J. Zhang, H. Hu, Z. Li, X. W. Lou, Double-Shelled nanocages with cobalt hydroxide inner shell and layered double hydroxides outer shell as high-efficiency polysulfide mediator for lithium-sulfur batteries. *Angew. Chem. Int. Ed. Engl.* **55**, 3982–3986 (2016).

57. G. Zhou, Y. Zhao, A. Manthiram, Dual-confined flexible sulfur cathodes encapsulated in nitrogen-doped double-shelled hollow carbon spheres and wrapped with graphene for Li–S batteries. *Adv. Energy Mater.* **5**, 1402263 (2015).

58. G. Zhou, Y. Zhao, C. Zu, A. Manthiram, Free-standing TiO$_2$ nanowire-embedded graphene hybrid membrane for advanced Li/dissolved polysulfide batteries. *Nano Energy* **12**, 240–249 (2015).

59. H. J. Peng et al., 3D carbonaceous current collectors: The origin of enhanced cycling stability for high-sulfur-loading lithium–sulfur batteries. *Adv. Funct. Mater.* **26**, 6351–6358 (2016).

60. G. Luengo, J. Aracil, R. G. Rubio, M. Diaz Pena, Bulk and surface thermodynamic properties in mixtures of small rigid molecules: The carbon tetrachloride+ carbon disulfide system. *J. Phys. Chem.* **92**, 228–234 (1988).

61. R. Legtenberg, H. A. Tilmans, J. Elders, M. Elwenspoek, Stiction of surface micromachined structures after rinsing and drying: Model and investigation of adhesion mechanisms. *Sens. Actuators A Phys.* **43**, 230–238 (1994).

62. J. Li, C. Rulison, J. Kiggans, C. Daniel, D. L. Wood, Superior performance of LiFePO4 aqueous dispersions via corona treatment and surface energy optimization. *J. Electrochem. Soc.* **159**, A1152–A1157 (2012).